



JGR Earth Surface



RESEARCH ARTICLE

10.1029/2021JF006544

Key Points:

- · Sediment flux in deforming till varies non-monotonically with effective
- The relationship between sediment flux and the speed of basal ice is nearly linear
- Coupling between ice and till causes the grain velocity profile of the bed to scale with slip speed

Supporting Information:

Supporting Information may be found in the online version of this article.

Correspondence to:

D. D. Hansen. ddhansen3@wisc.edu

Hansen, D. D., & Zoet, L. K. (2022). Characterizing sediment flux of deforming glacier beds. Journal of Geophysical Research: Earth Surface, 127, e2021JF006544. https://doi. org/10.1029/2021JF006544

Received 5 DEC 2021 Accepted 17 MAR 2022

Characterizing Sediment Flux of Deforming Glacier Beds

D. D. Hansen¹ and L. K. Zoet¹

¹Department of Geoscience, University of Wisconsin-Madison, Madison, WI, USA

Abstract Deformation of subglacial sediment during basal slip shapes the beds of many fast-flowing glaciers and ice streams. The resultant sediment flux impacts glacier dynamics and rates of subglacial erosion over a range of timescales, but its fundamental dependencies are not well understood. Using a cryogenic ring shear device, we conducted experiments to investigate the effects of both effective stress and slip speed on rates of till transport. Sediment fluxes were computed using digital image correlation from a photographic time series of the till bed. We find a near-linear relationship between sediment flux and slip speed, but a non-monotonic, double-valued dependency of sediment flux on effective stress. Deformation primarily occurred in a thin shear band near the ice sole, the thickness of which could vary with both parameters. Coupling between ice and till increased at higher slip speeds and effective stresses and scaled the magnitude of the flow profile.

Plain Language Summary Rapid motion of many glaciers and ice streams occurs by ice sliding over soft sediment beds. This sediment is mobilized in response to stress exerted by the overriding ice, which influences rates of erosion and generates subglacial landforms over a range of timescales. However, the physical processes that control this sediment flux are poorly understood largely due to the difficulty of isolating the influence of specific variables in the field. We address this uncertainty with a custom ring shear device capable of simulating glacier slip in the laboratory at realistic pressures, temperatures, and ice speeds. We tested the influence of two key parameters on sediment deformation—the slip speed of ice and the pressure exerted by the ice on the bed—and computed the rates of sediment transport using an image processing technique called digital image correlation. We find a near-linear relationship between sediment flux and slip speed, but a nonlinear relationship with ice pressure. Sediment deformation was mostly concentrated in a thin zone near the ice-sediment interface. Coupling between ice and sediment increased at faster ice velocities and higher ice pressures, which scaled sediment transport rates.

1. Introduction

Rapid motion of many glaciers and ice streams is facilitated by glaciers sliding over unconsolidated, water-saturated sediment or "till" (Kamb, 2001). As this weak sediment deforms in response to the overriding ice, it is redistributed at the ice-bed interface or evacuated from the system, reshaping the evolving subglacial landscape. This sediment flux alters the stability of ice streams (Alley et al., 2007; Bart et al., 2017; Simkins et al., 2018), affects subglacial hydrology (Damsgaard et al., 2016), and generates many of the iconic glacial landforms exposed by paleo ice sheets (Zoet et al., 2021) and observed beneath modern glaciers (King et al., 2009). Thus, the erosion, transport, and deposition of basal till are important controls on glacial landform development and ice sheet dynamics, and accurate estimates of till flux are a necessary component of predicting ice sheet stability.

For soft-bedded glaciers, subglacial sediment flux is partitioned between actively deforming till (Iverson, 2010), material entrained in basal ice (Rempel, 2008), and fluvial transport (Alley et al., 2003). The relative contribution of these processes to the overall sediment budget, however, is poorly constrained for many subglacial environments. With respect to sediment in transit through a till bed, which is the focus of this study, till flux is a function of the skin depth of deformation, the magnitude of strain, and the strain distribution in the sediment column. Deformation is often greatest at the ice-bed interface and decreases monotonically with depth to form a convex-upward profile. Field estimates for skin depth of deformation, however, range from centimeter (Engelhardt & Kamb, 1998) to meter scale (Boulton & Hindmarsh, 1987), provoking a long-running debate on the dominant controls on the strain profile and hence sediment flux. Numerous mechanisms have been proposed as likely candidates, including intrinsic physical properties of the till itself, such as the grain size distribution, GSD (Tulaczyk, 1999; Zoet & Iverson, 2020), effective stress (Iverson & Iverson, 2001), strain rate (Boulton & Hindmarsh, 1987), transient stress conditions that cause the locus of shear to migrate over time (Damsgaard et al., 2020; Iverson et al., 1998; Tulaczyk et al., 2000), or coupling between ice and till at their contact (Tulaczyk, 1999; Zoet

© 2022 The Authors.

This is an open access article under the terms of the Creative Commons Attribution-NonCommercial License, which permits use, distribution and reproduction in any medium, provided the original work is properly cited and is not used for commercial purposes.



& Iverson, 2020). However, little physical evidence exists to support or refute these claims, much less isolate their relative influence on the sediment budget.

Nevertheless, despite this uncertainty, two persistent assumptions within the fields of glaciology and glacial geology are that sediment flux, Q_{sed} , scales with ice pressure (Fowler & Chapwanya, 2014; Schoof, 2007) and the slip speed of basal ice, v_{ice} (Clark, 1993). Wide-ranging and in many instances conflicting dependencies of Q_{sed} on the effective stress, N (ice pressure, P_i , minus pore water pressure, P_w), and v_{ice} exist in the literature. The scaling between Q_{sed} and N arises in models that ascribe a viscous rheology to till (Hindmarsh, 1998) or assume till deforms plastically as a Coulomb material (Iverson & Iverson, 2001), and it serves as a foundational component for instability theories relating to the origin and elongation of subglacial bedforms (Fowler, 2010). However, studies that directly investigate the relationship between N and Q_{sed} are few and their results are contradictory. Numerical shear experiments with SPHERE, a 3D discrete element model, demonstrated an increase in shear zone width with increasing overburden pressure for the case of idealized spheres, providing support for a positive $N-Q_{\rm sed}$ relationship (Damsgaard et al., 2013). More recent experiments with the same model under different boundary conditions, however, show a "double-valued" trend between N and shear band thickness (and by extension $Q_{\rm sad}$), in which the depth of deformation increases to maximum around N = 60 kPa before decreasing at higher stresses (Kasmalkar et al., 2021). Furthermore, Boulton and Dobbie (1998) reported an inverse trend for split-cell ring shear experiments on two subglacial tills, though they did not explicitly state their boundary conditions or results. Their observation that shear zones were wider at low stresses (and faster strain rates) aligns with the inverse relationship between stress and shear band thickness commonly reported in the geotechnical literature (Desrues & Viggiani, 2004). Friction between ice and till at their contact adds another layer of complexity as well. During a series of soft-bed deformation experiments beneath Engabreen Glacier, Iverson et al. (2007) investigated the response of a synthetic till wedge to variable N by pumping water through the system and monitoring deformation with buried tilt meters. Minimal deformation (and by extension low Q_{sed}) was inferred at both low and high stresses with a maximum occurring in-between—behavior they attributed to a trade-off between the frictional strength at the interface as grains became submerged by a thin water layer and the strength of grain-grain contacts in the till bed.

The association of elongate bedforms with areas of fast glacier flow in relic glacier flow fields (Stokes & Clark, 2002) and beneath modern ice streams (King et al., 2009) also led some to suggest a link between $Q_{\rm rad}$ and v_{icc} ; however, the Coulomb nature of till renders the mechanism for such a relationship unsubstantiated. Zoet et al. (2021) showed a statistically significant correlation between elongation ratio of subglacial bedforms and cumulative slip displacement for a drumlin field shaped by the Green Bay Lobe of the Laurentide Ice Sheet, providing evidence for a dependence of Q_{sed} on v_{ice} , but the process driving this relationship was purely assumed and based on no known mechanism. Couette cell experiments on granular materials show that the maximum velocity in a shear band can scale with the velocity of a shearing boundary (Mueth et al., 2000). However, coupling between ice and till is likely lowest at high basal water pressures—coincidentally when sliding velocities are at their maximum. This would seemingly preclude a one-to-one scaling relationship, meaning the subglacial $Q_{\rm sed}$ - $v_{\rm ice}$ relationship is more nuanced than that of a purely granular system, owing to the complexities of ice-bed coupling. Additionally, Zoet and Iverson (2020) demonstrated a velocity-dependent transition between form drag (i.e., ice sliding around clasts lodged at the interface) and skin friction (i.e., till deforming at depth) that depends on the sliding velocity, the stress state, and the GSD of the till. In their conceptual model, minimal deformation occurs below a threshold slip speed (their Equation 2), opening the possibility for nonlinearity in the v_{ior} - Q_{sed} parameter space.

Despite being of central concern for the fields of both glaciology and glacial geology—and in many ways, the primary process linking these two fields—the rates and dependencies of subglacial till deformation are very much unresolved. Considered together, the body of prior work presents a conflicting patchwork of hypotheses and observations that offers no clear path forward, despite the high scientific and societal relevance of this problem. Quantitatively linking these two disciplines begins with developing a fundamental understanding of till flux and its dependencies therein. To date, monitoring deformation in glaciogenic sediments in response to systematic variations in slip speed and effective stress has not been possible largely due to the inaccessibility of the ice-bed interface and the absence of a suitable experimental protocol that allows for a thorough interrogation of the dependencies of $Q_{\rm sed}v_{\rm ice}$. Consequently, only a portion of the full picture has been observable in any one instance, producing a wide array of observations that are seemingly at odds with one another.

HANSEN AND ZOET 2 of 18

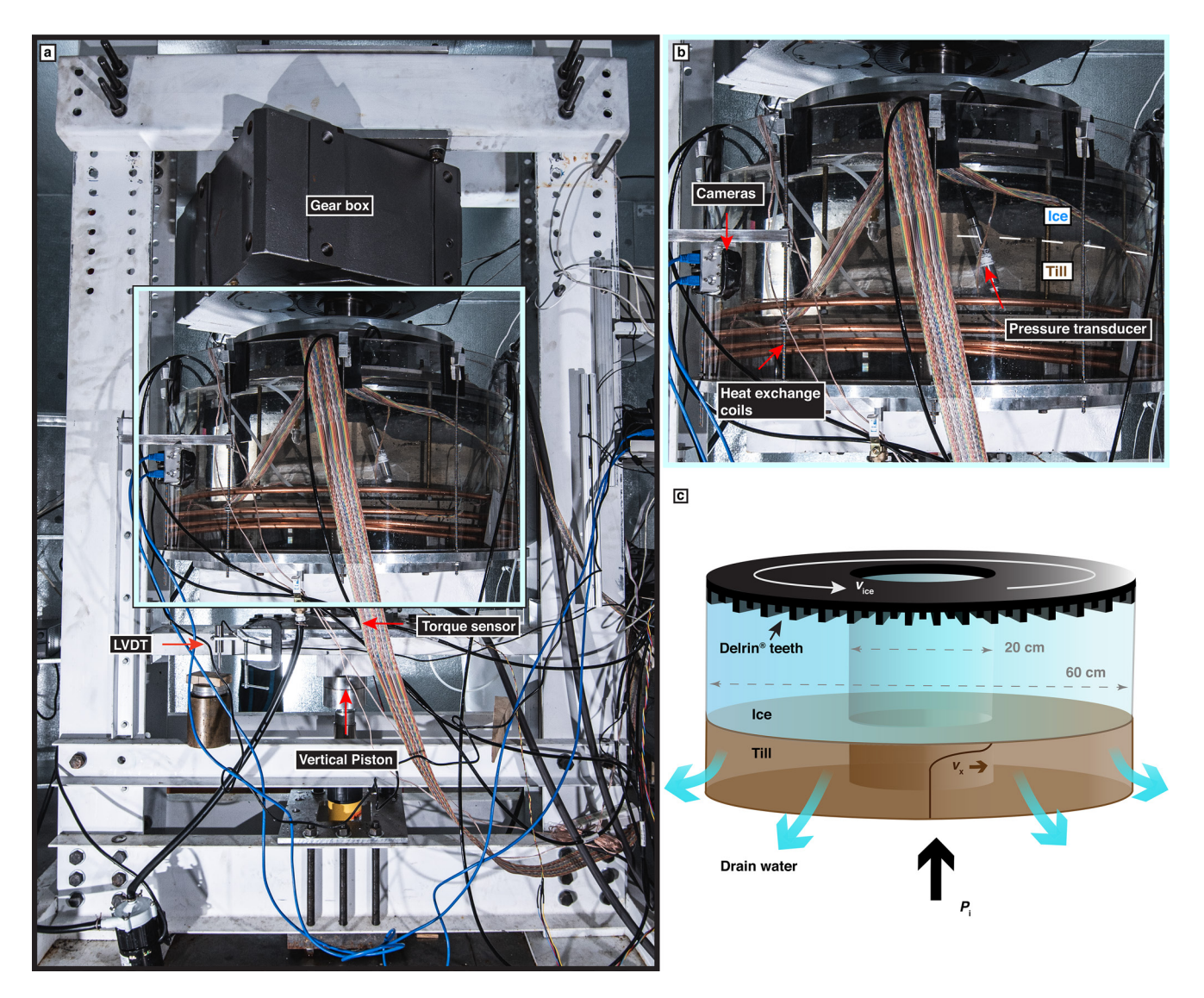


Figure 1. Experimental setup. (a) A photograph of the cryogenic ring shear device. The sample chamber is suspended between vertical I-beams that make up the load frame. Pressure, P_i , is applied by a vertical piston that presses the ice ring into a bed of subglacial till. A motor connected to the gear box rotates the top platen at a prescribed velocity, v_{ice} , which grips the ice ring with a series of irregular Delrin® teeth. As the ice ring slides over the till bed, a torque sensor attached to the base of the sample chamber measures the resultant drag. (b) An enlarged cutaway of the sample chamber showing ice sliding over subglacial till. Cameras mounted to the outer wall monitor movement in the till bed, and three pressure transducers measure pore water pressure, P_w , in the sediment. Twelve drainage lines evacuate water from the pore space in the till. (c) A schematic of the sample chamber illustrating various experimental parameters. Grains in the till move horizontally at speed, v_x (curved brown line), in response to stress exerted by the overriding ice (Photo credit: Ethan Parrish).

We address the uncertainty surrounding the influence of N and $v_{\rm ice}$ on $Q_{\rm sed}$ using a novel, large-diameter, cryogenic ring shear device with a transparent sample chamber, recently constructed at the University of Wisconsin–Madison (Figure 1). To explore the dependencies of $Q_{\rm sed}$, we slid rings of temperate ice over a till bed at realistic subglacial conditions. With this experimental setup, we systematically varied N and $v_{\rm ice}$ by changing the load applied to the ice ring and its rate of rotation, respectively. We quantified the resultant deformation using digital image correlation (DIC) on a photographic time series of the till bed. We find clear, though importantly not always monotonic, dependencies of $Q_{\rm sed}$ on N and $v_{\rm ice}$ —thereby experimentally addressing this problem in the coupled ice-sediment system for the first time.

HANSEN AND ZOET 3 of 18



2. Materials and Methods

2.1. Experimental Design

To simulate basal slip, we used a cryogenic ring shear device (Figure 1) to slide a ring of ice under an axial load (60-cm outer diameter, 20-cm inner diameter, and initially \sim 15-cm thick) over an \sim 11-cm-thick bed of till. The annular sample chamber was submerged in a temperature-controlled bath of glycol and water, regulated with a Lauda PRO 245 E circulator capable of O($10^{-2\circ}$ C) precision. To create the ice ring, deionized water was frozen and crushed to create an aggregate of ice granules, which were added to the sample chamber as \sim 5-cm-thick layers, submerged with deionized water, and allowed to freeze. This process was repeated sequentially until the ice reached its target thickness. A single strand of beads was frozen in the ice near the outer perimeter to track cumulative ice deformation throughout the experiment (which was negligible). Once the ice ring was created, it was removed from the sample chamber so the till bed could be built in place.

Prior to loading, sediments were passed through a 9.51-mm mesh sieve, which is less than one-tenth the thickness of the bed in accordance with standard geotechnical protocols (Head, 1989). (The GSD is described in Supporting Information S1.) After the till was added to the sample chamber to the appropriate thickness, we leveled its surface and tamped it firmly with a rubber mallet to minimize excess void space. Four stacks of sequentially numbered beads were installed in the bed to track cumulative strain (two at the centerline and two at the outer perimeter), so that they spanned the full depth of the till and the top bead is roughly level with the ice-bed interface. Deionized water was then added to the sample chamber until the till was completely saturated, and the ice ring was lowered on top of it. A hydraulic press raised the sample chamber in place so that the ice ring contacted the Delrin[®] teeth of the upper platen, and a layer of chilled deionized water was poured onto the top surface of the ice to couple the ice ring to the rotating platen once it froze. One consideration at this stage of the experiment was maintaining a temperature profile in the sample chamber that allowed the ice to freeze to the Delrin® teeth while maintaining the pressure melting point at the ice-bed interface and till bed. To facilitate this, we dropped the level of the glycol bath to a position midway up the ice ring and held its temperature above freezing, while setting the ambient freezer temperature to -4° C. Once the ice ring was frozen in place and coupled to the Delrin[®] teeth, the bath level was raised to the top of the ice ring and warmed to ~0.04°C, which ensured that the ice remained temperate and meltwater freely drained from the till without flash freezing in the drainage lines. At this stage, the motor was engaged. Adhesive-backed rubber installed at the base of the sample chamber minimized slip of the till along the bottom boundary during the experiments.

As the top platen rotated, spinning the ice ring over the till bed, axial load was applied via an ISCO 100DM syringe pump, capable of maintaining a pressure within approximately ± 0.2 kPa. Resistance to shear is measured by a custom-built torque sensor mounted at the base of the sample chamber, and pore water pressure in the till was measured with three Omega pressure transducers mounted ~ 7 cm below the ice-bed interface in the sidewall. Twelve drainage lines connected the sample chamber to atmospheric pressure, and twelve-glass bead thermistors installed in the sidewalls of the sample chamber recorded temperature throughout the experiment. The GSD of the till was measured using laser diffractometry for grains smaller than 1 mm and manually sieved to determine the size fractions between 1 and 9.51 mm (see Supporting Information S1 for details).

2.2. Variable Sliding Velocity and Effective Stress

We assessed the influence of effective stress and sliding velocity on deforming Horicon till—a sandy, subglacial diamicton deposited by the Green Bay lobe of the Laurentide Ice Sheet (Mickelson & Syverson, 1997)—and collected data during two experiments. For the first experiment, we successively applied four effective stresses, $N \sim 8$, ~ 22 , ~ 50 , and ~ 113 kPa, while implementing velocity steps throughout. In the event that variable water pressure led to slight differences in N between successive steps ($\lesssim 2$ kPa difference), we report the average of the set for clarity when referring to the group (see Table 1).

At $N \sim 22$ kPa, we implemented four velocities sequentially ($v_{\rm ice} = 25$, 50, 100, and 300 m/yr), and for $N \sim 50$ and ~ 113 kPa, we conducted a single velocity step from 100 to 300 m/yr. Finally, we measured a single effective stress ($N \sim 199$ kPa) in the second experiment at $v_{\rm ice} = 100$ m/yr. Reported velocities represent the speed at the outer boundary of the cylindrical sample chamber. After each change in velocity or stress, we allowed the system to reach critical state deformation, at which point shear stress remained relatively constant (Figure 2). Following

HANSEN AND ZOET 4 of 18



Table 1 Experimental Properties for Each Stress and Velocity Step ^a						
v _{ice} (m/yr)	P_{i} (kPa)	$P_{\rm w}$ (kPa)	N (kPa)	num _{data}	$num_{\rm pic}$	$Q_{\rm sed}$ (m ³ /yr)
100	10.7 ± 0.0423	2.36 ± 0.0591	8.35 ± 0.0053	6,602	111	0.351 ± 0.0238
25	28.9 ± 0.381	5.98 ± 0.152	22.9 ± 0.168	15,897	264	0.0752 ± 0.0070
50	28.6 ± 0.0584	5.62 ± 0.0586	23.0 ± 0.0068	10,561	176	0.203 ± 0.0154
100	28.0 ± 0.092	5.83 ± 0.070	22.2 ± 0.0134	23,041	384	0.510 ± 0.0434
300	27.9 ± 0.0410	6.74 ± 0.208	21.2 ± 0.0449	7,681	197	1.51 ± 0.153
100	83.5 ± 0.166	33.2 ± 0.238	50.4 ± 0.0835	27,601	260	0.661 ± 0.0434
300	83.8 ± 0.0392	33.6 ± 0.154	50.2 ± 0.0253	8,881	149	1.99 ± 0.0959
100	174.4 ± 0.0660	60.8 ± 0.692	113.6 ± 0.4832	23,337	389	0.576 ± 0.0425
300	174.4 ± 0.0345	63.0 ± 0.346	111.4 ± 0.1209	6,840	104	1.62 ± 0.147
100	241.8 ± 1.060	42.6 ± 0.793	199.2 ± 1.751	25,006	418	0.473 ± 0.0334

^aIce velocity, v_{ice} ; mean overburden pressure, P_i ; mean pore water pressure, P_w ; mean effective stress, $N = P_i - P_w$; number of samples (acquired at 1 s intervals), num_{data} ; number of photographs used for DIC calculation (acquired at 1-min intervals), num_{pic} ; and sediment flux, Q_{sod} . We state corresponding standard deviations and propagated uncertainty as " \pm ."

a change in axial load, the path to critical state could take a day or longer but was generally on the order of 1 hr following a change in velocity. Values for *N* reported herein represent the average normal stress over a chosen interval minus the average water pressure recorded by the three transducers installed near the till bed.

2.3. Digital Image Correlation

We estimate rates of till deformation using 2D DIC, an image processing technique that quantifies displacement occurring in a plane orthogonal to the camera axis (Figure 3). DIC compares the grayscale intensity of two digital images (a "reference image" and a "secondary image") captured at discrete moments in time to identify the position of maximum correlation. For an 8-bit image, pixels are assigned a numerical value between 0 (pure white) and 255 (pure black), and the reference image is split into a series of subsets of prescribed dimensions.

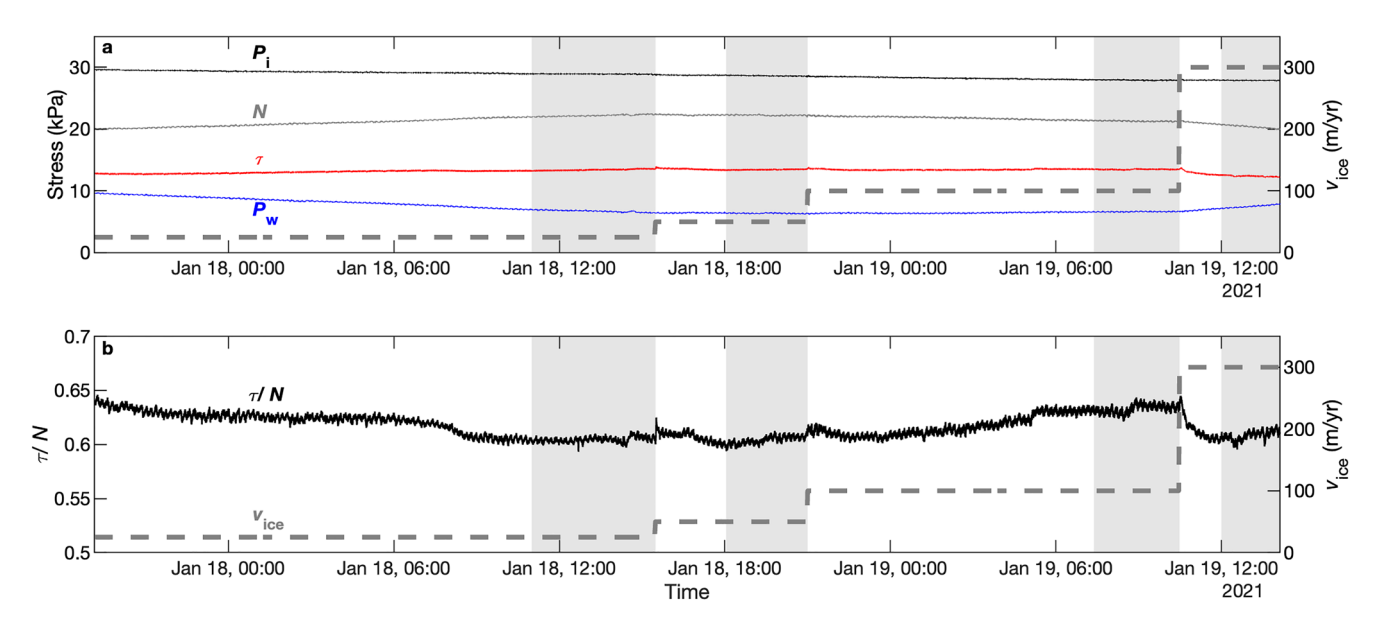
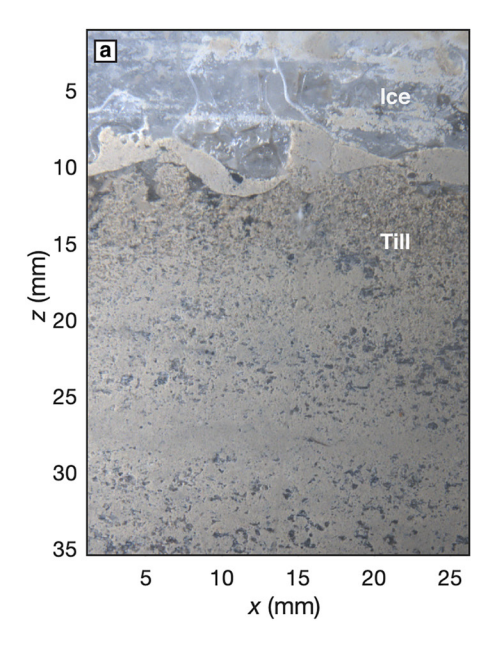


Figure 2. (a) Representative time series showing the evolution of four experimental parameters: applied ice pressure (P_i) , average water pressure recorded in the till (P_w) , effective stress $(N = P_i - P_w)$, and basal shear stress, τ , over the course of four different slip speeds $(v_{ice} = 25, 50, 100, \text{ and } 300 \text{ m/yr})$. Dashed gray lines are the prescribed ice velocity in both plots, and the shaded regions indicate windows of data used for subsequent calculations. We select periods in which τ remains relatively constant, assuming critical state deformation. (b) The coefficient of friction, presented as τ/N , calculated over this same period.

HANSEN AND ZOET 5 of 18



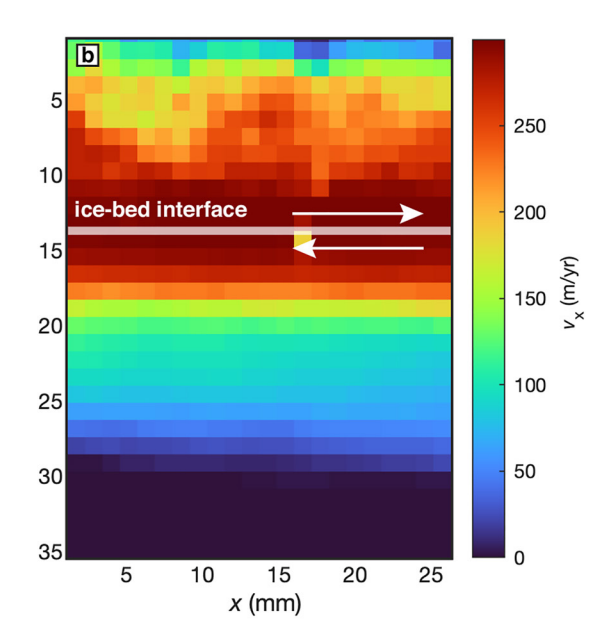


Figure 3. (a) Example photograph showing a camera field of view. (b) Mean horizontal velocities (v_x) computed using digital image correlation from a photographic time series for an interval with $N \sim 50$ kPa and $v_{ice} = 300$ m/yr (see also Movie S1). The white line designates where we infer the position of the ice-bed interface, and the two white arrows convey the sense of shear. (Lower velocities above the ice-till boundary reflect poor correlation due to the photographic texture of the ice surface rather than the actual ice speed and are not considered in any calculations).

An algorithm then searches a larger region of interest defined on the secondary image to identify the position of maximum correlation for each subset. Displacement is computed as the difference between the original position of the subset and this correlation maxima, and given the time interval between images, the local velocity vector can be determined.

For this study, we used a MATLAB routine developed by Bickel et al. (2018), which is freely available online (https://github.com/bickelmps/DIC_FFT_ETHZ) and implements a fast Fourier transform correlation approach. Images were co-registered to an accuracy of 0.5 pixels (Guizar-Sicairos et al., 2008), and a vector post-processing filter was applied at the conclusion of each DIC run to eliminate spurious results greater than 1/3 the dimension of the interrogation window. DIC algorithms are sensitive to image texture patterns (Crammond et al., 2013) with finer speckles and a high degree of randomness typically producing the best results (Barranger et al., 2010). Since the till used in these experiments was largely homogenous in color, we seeded it with black sand (~10% by weight) to increase contrast and improve feature tracking.

Digital images, sized 2,048 × 1,536, were acquired with two vertically stacked FLIR digital cameras, equipped with Edmund Optics F1.4 lenses with a 25-mm focal length. These cameras were mounted against the outer acrylic wall of the glycol/water bath, and two strips of white LED lights angled against the outer wall of the sample chamber illuminated the photographic surface. The field of view of the cameras overlapped by ~ 123 pixels in the first experiment and ~330 pixels in the second. All images are acquired at 1-min intervals. For 2D DIC, the camera's line of site (LOS) should ideally be oriented perpendicular to the field of deformation. However, this was not strictly possible in our experiments due to the cylindrical geometry of the sample chamber. Error introduced by out-of-plane deformation is influenced by the degree of curvature of the deformation field in the camera's field of view. For our setup, the maximum tangent angle between the chamber wall and a plane perpendicular to LOS was $\sim 1.3^{\circ}$, which introduces error on the order of 0.01 pixels (or ~ 150 nm) (Meng et al., 2006). Given the scope of our experiments, uncertainty at this scale is negligible, and the deformation field can be approximated as planar. Pixel dimensions for each set of images were determined from photographs of a 1-mm-scale grid placed flush against the chamber wall in the cameras' field of view. For the first and second experiments, the corresponding pixel dimensions were $\sim 1.78 \cdot 10^{-5}$ m for both the top and middle cameras. For the second experiment, the pixel dimensions were $\sim 1.89 \cdot 10^{-5}$ m and $\sim 1.91 \cdot 10^{-5}$, respectively. Differences in pixel dimensions arose due to slightly different positions of the camera mount or focus between the respective experiments. Lens distortion at this scale was negligible.

HANSEN AND ZOET 6 of 18



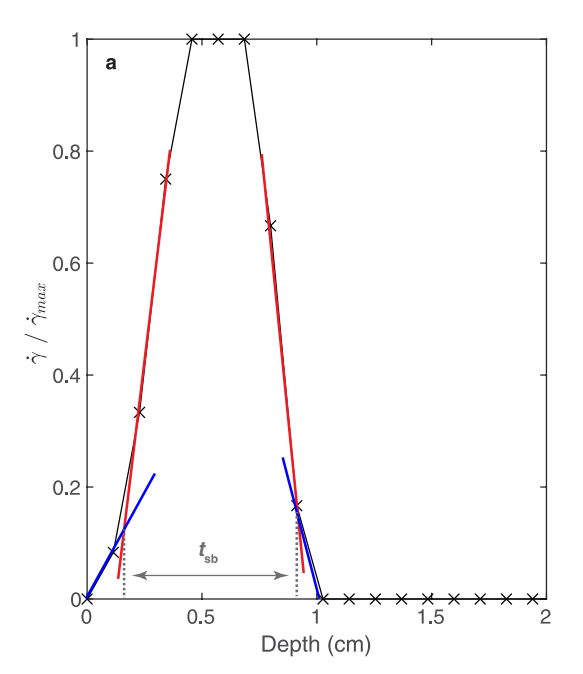
An important consideration when setting up a DIC run is setting the optimal size of the search window. With respect to the dimensions of this subset, a trade-off exists between the desired accuracy of the estimated displacement and the resolution of the displacement field. Larger search windows ensure a good signal-to-noise ratio but sacrifice accuracy as the estimates are averaged over a larger correlation window, and the converse is true for smaller window sizes. Based on their results with the same algorithm, Bickel et al. (2018) suggest that subsets should be 6-12 times greater than the expected displacement. In our image pairs, displacement is not constant through the field of view, but rather decreases from a maximum near the ice-bed interface with depth to zero and varies with different rotation rates. We implemented windows that were at least 6 times greater than the maximum displacement for most runs, except those conducted at $v_{\rm ice} = 300$ m/yr, which had a window that was at least 4 times greater. Photographs were taken at 1-min intervals throughout the experiments, and appropriate intervals were selected from this time series for each value of v_{ice} to perform the DIC analysis. For example, we used a 128-pixel interrogation window for photographs taken at $v_{\rm ice} = 100$ m/yr that contained the bulk of the shear band deformation, performed the DIC analysis for two sets of 2-min intervals in the same time window, and then averaged both sets to obtain the mean flow profile. This corresponds to a maximum displacement in each 2-min pair that was approximately 7-8 times smaller than the dimensions of the interrogation window. Data at the first column were discarded from subsequent calculations due to spurious edge effects as well as negative horizontal displacements measured during shear. During three stages of the experiment ($N \sim 50$ kPa at $v_{\rm ice} = 100$ m/yr, $N \sim 114$ kPa at $v_{\rm ice} = 100$ m/yr, and $N \sim 111$ kPa at $v_{\rm ice} = 300$ m/yr), a lighting malfunction produced dark images with low RGB pixel values, which diminished the quality of the correlation. Recorded data, however, were sufficient for the algorithm to estimate displacements at reasonable correlation criteria based on the translation invariant normalized root mean squared error (NRMSE) calculated for each displacement value (Guizar-Sicairos et al., 2008). Mean NRMSEs for the three darker periods were 0.19 (with corresponding standard deviation, $\sigma_{\text{NMRSE}} = 0.019$, and number of samples, n = 138,000), 0.19 ($\sigma_{\text{NMRSE}} = 0.019$; n = 112,320), and 0.19 ($\sigma_{\text{NMRSE}} = 0.021$; n = 67,800), respectively; whereas mean NMSREs for all other intervals ranged between 0.04 and 0.10.

2.4. Estimating Shear Band Thickness

There is no single agreed upon criterion to determine the thickness of a shear band, $t_{\rm sh}$, in a granular material (Alshibli & Sture, 1999; Rattez et al., 2020; Rechenmacher & Finno, 2004; Soltanbeigi et al., 2020; Zhu et al., 2016). Shear bands are characterized by a loss of homogeneity in the deformation field that concentrates excessive shear strain and dilatancy in a thin band. Thus, attempts to delineate their boundaries using experimental data often focus on how these two parameters vary across a cross section of the shear band with respect to the surrounding medium. Dilatancy is poorly constrained in our experiments. Shear strain rate profiles, however, can be computed from the DIC-derived displacement data, and these provide a qualitative means to demarcate the boundaries of the shear band without prior knowledge of the void ratio during shear.

We adopt an approach developed by Soltanbeigi et al. (2020), who suggest that the boundaries of a shear band can be approximated as the inflection points on a cross-sectional strain profile of the shear band (Figure 4). Our workflow can be summarized as follows: First, we calculate the spatial derivatives of the velocity vectors derived for each image pair in the time series using the central difference for interior data points and a single-sided difference method for gradients at the boundaries. We then calculate the shear strain rate, a component of the 2D small strain rate tensor, for each image pair from the velocity gradient. Median shear strain rate profiles are calculated from the time series, normalized by their maximum value, and then plotted against depth to form a cross-sectional shear strain rate intensity profile. The criteria for estimating shear band width in this parameter space (i.e., "method II" in Soltanbeigi et al., 2020) can be summarized succinctly as: (a) fitting tangents to the two tails of the profile where the rate of strain change is approximately constant, (b) fitting tangents to the linear regions of the curve between the tails and the peak, (c) locating the points of intersection for both sets of tangent lines, and then (d) measuring the distance between these two points of intersection on either side of the shear band—this value is presumed to be $t_{\rm sb}$. An advantage of this method with respect to our data is that it does not rely on the assumption of a Gaussian distribution of shear strain, since distributions were bimodal at certain stages of the experiments (Figure 4b).

HANSEN AND ZOET 7 of 18



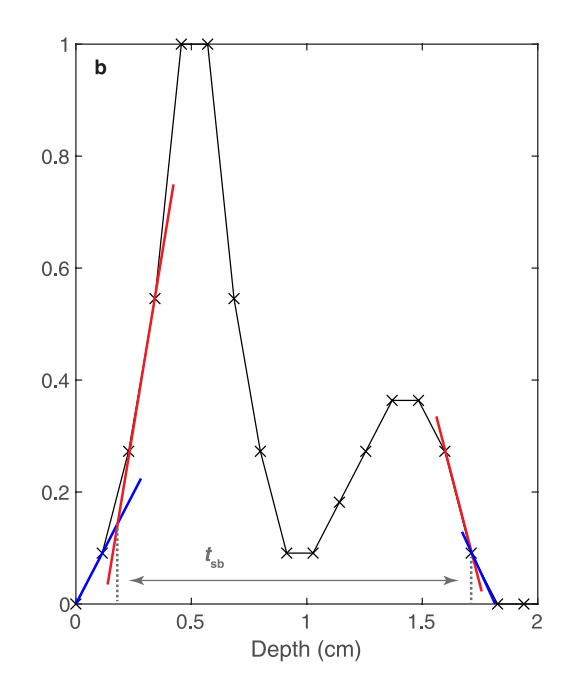


Figure 4. Method for determining shear band thickness, t_{sb} , using the shear strain rate intensity profile (i.e., median shear strain rate, $\dot{\gamma}$, normalized by its maximum value, $\dot{\gamma}_{max}$) for both (a) single peak and (b) bimodal distributions. We identify the intersection between tangents fit to the linear regions between the curve and the peak and the tails of the profile where the rate of change is approximately constant. t_{sb} is the distance between the two intersections. Depth here denotes distance from the inferred ice-bed interface.

2.5. Estimating Sediment Flux

We calculate sediment flux by numerically integrating time-averaged 1D horizontal velocity profiles computed from the DIC time series using the trapezoidal rule (Scott, 2011). Unlike our calculations for shear band thickness, we aim to include the totality of grain motion that occurs in response to the overriding ice. A complicating factor in these calculations is that the ice-bed interface is occasionally obscured from the cameras' field of view by a thin layer of sediment squeezed between ice and acrylic at the outer boundary of the sample chamber. For some steps, a clear demarcation between ice and till can be inferred from the flow profiles due to a sharp inflection point in the horizontal velocities that corresponds to vertical position with zero shear strain rate. For other steps, this distinction is not as apparent from the mean horizontal velocity profiles alone, so we use the optical record in conjunction with these data to clarify the position of the ice-bed interface.

3. Results

3.1. Shear Band Morphology

Mean horizontal velocity (v_x) profiles computed from the DIC time series show that steady-state deformation in the till bed was primarily concentrated in a thin band near the ice sole ~0.7–2.5 cm thick where particle velocities decreased monotonically with depth (Figure 5 and Figures 8b, 8d and 8f). The morphology of the v_x profiles varied though most do not resemble the canonical "concave-down" exponential decay in velocity with depth. Rather, many resemble an error function, similar to velocity profiles reported in DEM simulations (Damsgaard et al., 2013) and numerous soft matter experiments in Couette cell devices (Fenistein et al., 2004; Roy et al., 2019).

A common practice is to normalize shear band thickness, $t_{\rm sb}$, by the median grain size diameter, $D_{\rm 50}$, of the sediment ($D_{\rm 50} \sim 0.53$ mm for the till used in our experiments). Over the parameter range tested, $t_{\rm sb}/D_{\rm 50}$ ranged from ~11 to ~47. These values fall well within the overall spread recorded for plane strain deformation experiments, which are commonly reported between 5 and 15 but can vary by up to an order of magnitude or more for different materials and experimental setups (Wu et al., 2008). Rattez et al. (2020), for example, measured the thickness of shear bands produced during triaxial experiments on sediments with different GSDs and reported significantly

HANSEN AND ZOET 8 of 18

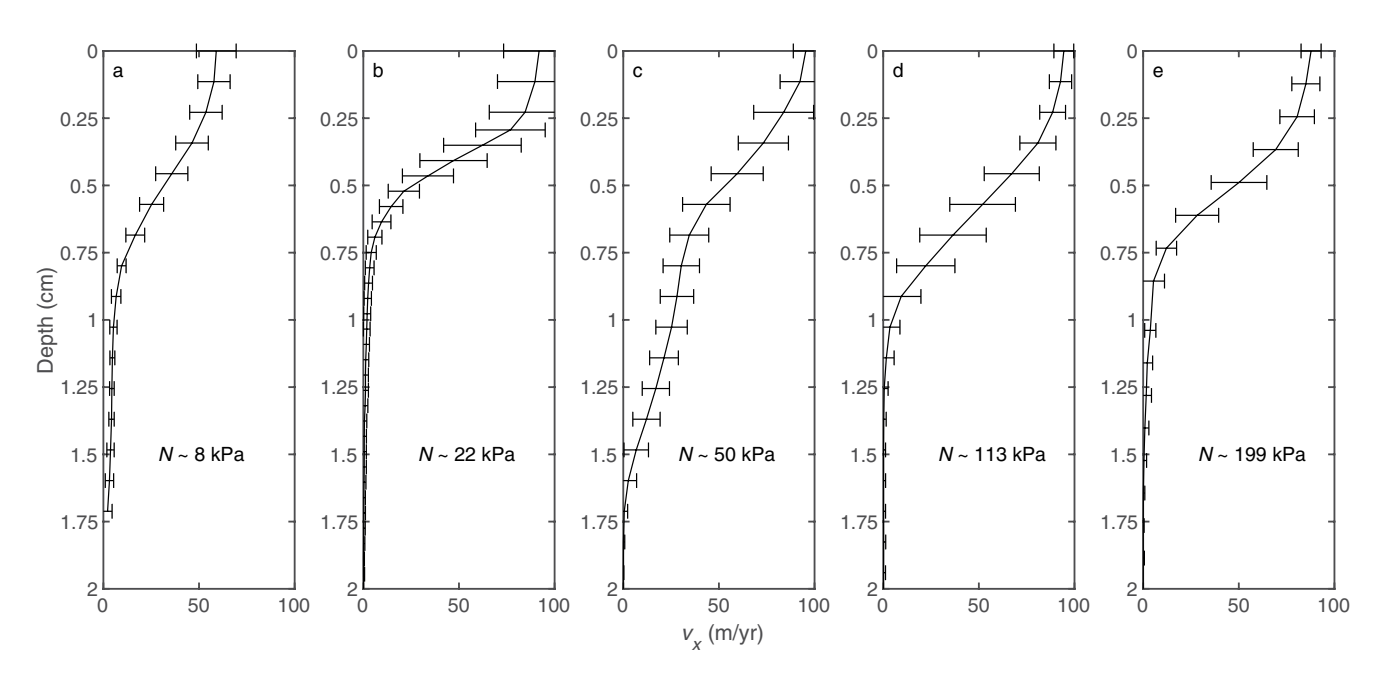


Figure 5. Five mean horizontal velocity profiles (v_x) computed from the digital image correlation time series for different effective stresses (N) at a single prescribed ice velocity $(v_{ice} = 100 \text{ m/yr})$. Deformation was largely concentrated in a thin zone near the ice-bed interface approximately 0.7–2.5 cm wide throughout the experiments. Depth denotes the vertical distance from the inferred ice-bed interface. Error bars show the standard deviation of horizontal velocities at each vertical position.

higher $t_{\rm sb}/D_{50}$ for sediments with fractal GSD, such as till, than for sediments with uniform granularity (16.7 compared to 10.3, respectively, in their experiment at a confining stress of 275 kPa).

3.2. Influence of Effective Stress on Sediment Flux

Mean v_x profiles computed for different values of N at two sliding velocities, $v_{\text{ice}} = 100$ and 300 m/yr initially show a widening zone of deformation with increasing N, but past a threshold value the deforming layer thins (Figure 5). The shear band at $N \sim 8$ kPa (Figure 5a) is the exception to this trend as deformation is slightly more distributed than the subsequent stage at $N \sim 22$ kPa (Figure 5b). This behavior likely reflects the evolution of the experiment over the first 2 days rather than an intrinsic characteristic of the $N-Q_{\text{sed}}$ relationship.

We compute the sediment flux at each N by integrating the 1D v_x profiles numerically with respect to depth. For this calculation, we assume unit width radially (directed into the ring away from the outer sample chamber wall) to report $Q_{\rm sed}$ in units of m³/yr (Table 1). Because the magnitude and vertical distribution of the particle velocities both contribute to $Q_{\rm sed}$, the variable coupling between ice and till introduces scatter in the $N-Q_{\rm sed}$ relationship though the rates of till transport are clearly elevated at the faster sliding speed. Dividing each velocity profile by its respective maximum v_x prior to integration normalizes the influence of velocity and allows for a direct comparison of the $N-Q_{\rm sed}$ trends at the two sliding speeds. With this correction applied, both sets of $N-Q_{\rm norm}$ data collapse along similar curves (Figure 6), in which $Q_{\rm norm}$ increases with increasing N from the point of flotation (N=0 kPa) to a maximum value around $N\sim 50$ kPa, before decreasing at higher stresses. This "double-valued" $N-Q_{\rm norm}$ relationship arises from the evolution of $t_{\rm sb}$ with the stress state. Figure 7 shows the variability of $t_{\rm sb}/D_{50}$ with N at two sliding speeds, $v_{\rm ice}=100$ and 300 m/yr. At $v_{\rm ice}=100$ m/yr, $t_{\rm sb}/D_{50}$ initially increases to a maximum ($t_{\rm sb}/D_{50}\sim 32$ at $N\sim 50$ kPa) before reducing at higher stresses.

3.3. Influence of Slip Speed on Sediment Flux

Velocity steps conducted at three different effective stresses demonstrate an increase in Q_{sed} with increasing v_{ice} (Figures 8a, 8c and 8e). For the velocity steps from 100 to 300 m/yr, we observed an approximately threefold increase (3.0×, 3.0×, and 2.8×, respectively) in Q_{sed} with a threefold increase in sliding speed at all three values of N. This proportionality is clearly reflected in a side-by side comparison of the normalized horizontal velocity

HANSEN AND ZOET 9 of 18

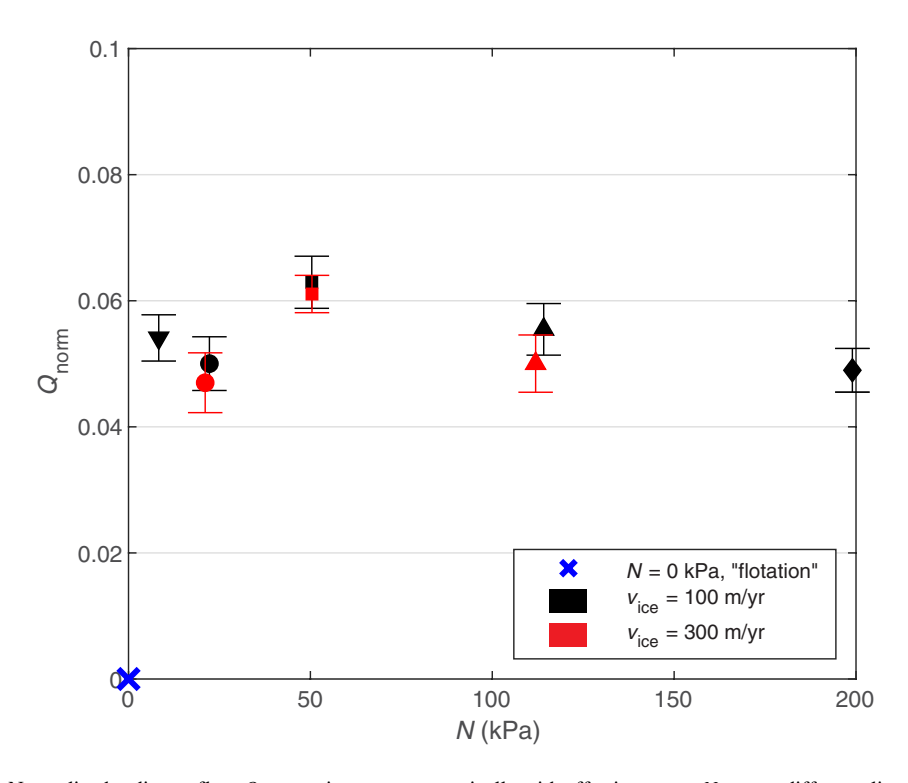


Figure 6. Normalized sediment flux, Q_{norm} , varies non-monotonically with effective stress, N, at two different slip speeds, v_{ice} . To obtain (dimensionless) Q_{norm} , mean horizontal velocity profiles (assuming unit width) were normalized by their maximum value and integrated with respect to vertical position, which was normalized by the thickness of the till bed. Error bars represent the normalized standard deviation of the horizontal velocity measurements, propagated through the integration. Horizontal error bars for N are smaller than the marker width. Marker shapes denote the stress state, and colors convey velocity. This classification scheme is maintained in all subsequent plots.

profiles (Figures 8b, 8d and 8f), which show little change in the relative vertical distribution of v_x at these speeds even though $v_{\rm ice}$ scales the magnitude of the flow profile. For the sliding speeds implemented at $N \sim 22$ kPa, which represent our most complete span of this parameter space, the $v_{\rm ice}$ – $Q_{\rm sed}$ relationship appears weakly nonlinear with a trendline that is offset from the origin based on its best-fit regression ($Q_{\rm sed} = 0.00886(v_{\rm ice} - 15.5)^{0.909}$). Between the windows of data selected for 25 and 100 m/yr, deformation localized from a zone distributed over ~ 2.5 cm with slightly irregular flow profiles to a thin shear band.

3.4. Ice-Till Coupling

Coupling between ice and till, presented here as the ratio between the maximum v_x in each flow profile and the slip speed of basal ice ($v_{\text{max}}/v_{\text{ice}}$), changed nonlinearly in response to both changing N and v_{ice} (Figures 9a and 9b). Increased N at a single slip speed ($v_{\text{ice}} = 100 \text{ m/yr}$) resulted in a steep increase in $v_{\text{max}}/v_{\text{ice}}$ from 0 to 22 kPa, followed by a nearly coupled interface at subsequent higher stresses (Figure 9a). Velocity steps implemented at $N \sim 22 \text{ kPa}$ produced a nonlinear increase in $v_{\text{max}}/v_{\text{ice}}$ as well (Figure 9b). For steps at $N \sim 50$ and $N \sim 113 \text{ kPa}$, the behavior at lower sliding speeds is not constrained, but coupling appears to have reached a maximum at 100 m/yr within estimated uncertainties.

4. Discussion

4.1. Shallow Deformation in Subglacial Environments

Till deformation in glacial settings occurs at depths that span orders of magnitude (Evans et al., 2006); however, the propensity for pervasive shearing to occur at steady-state conditions or solely in response to transient forcing is controversial. This uncertainty is further exacerbated by the lack of evidence for distributed deformation in the glacial geologic record, which suggests that shallow deformation dominates in subglacial environments

HANSEN AND ZOET 10 of 18

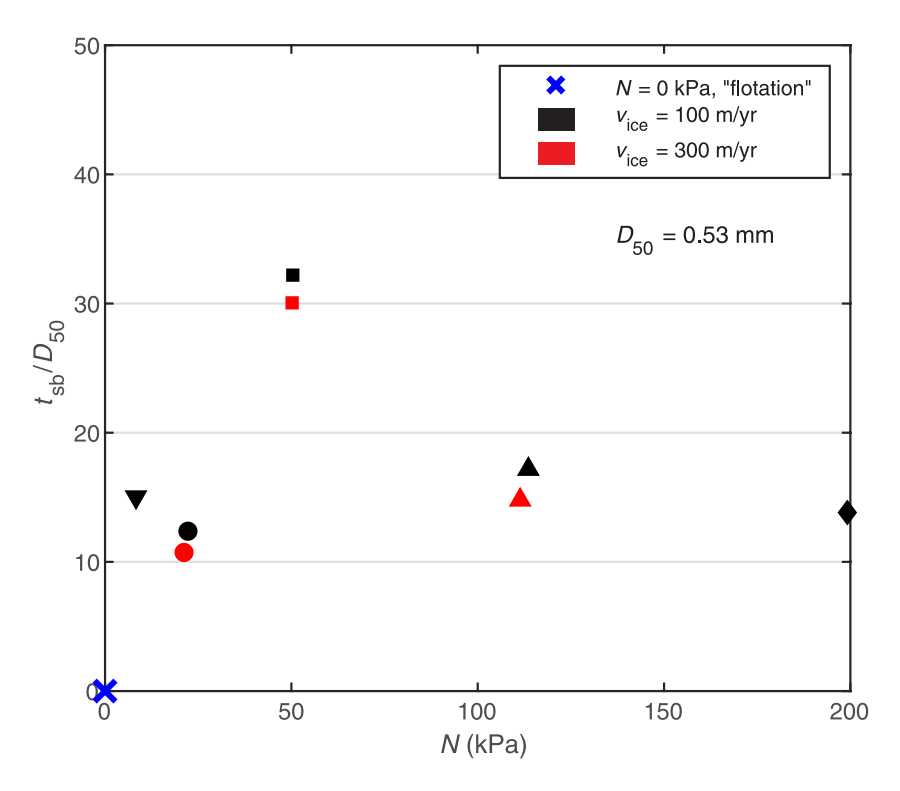


Figure 7. Relationships between estimated shear band thickness, $t_{\rm sb}$ (normalized by the median grain diameter of the sediment, $D_{\rm 50}$), and effective stress, N, plotted for two ice velocities. Horizontal error bars for N are smaller than the marker width.

(Piotrowski et al., 2001). Our results add further support to the hypothesis that steady-state deformation in fine-grained or sandy subglacial till is largely accommodated in a thin shear band near the ice sole. Additional factors—such as a coarser GSD (Rattez et al., 2020), the presence of plowing clasts or ice keels at the ice-bed interface (Tulaczyk et al., 2001), or a migrating failure plane due to a transient evolution in *N* (Damsgaard et al., 2020; Iverson et al., 1998; Tulaczyk et al., 2000)—may drive deformation deeper, but in their absence, shallow deformation dominates. This finding is consistent with Engelhardt and Kamb's (1998) inference of a thin shear band beneath an Antarctic ice stream where significant variation in *N* is uncommon and the ice slides over fine-grained till (Tulaczyk et al., 1998).

Because our results pertain to a single GSD, it is instructive to consider how trends may vary for tills with contrasting granulometry. Few data exist regarding the scaling relationship between $t_{\rm sb}$ and D_{50} for sediments with fractal GSD (Rattez et al., 2020; Tulaczyk, 1999). Our expectation for deforming till, based on recent experimental work by Rattez et al. (2020), is that $t_{\rm sb}$ covaries with D_{50} , but the magnitude of $t_{\rm sb}/D_{50}$ correlates inversely with the degree of grain uniformity. A caveat with respect to the subglacial system, however, is that this relationship may break down for tills where ice velocities are too slow to mobilize sediment particles at the interface (Zoet & Iverson, 2020). Future work exploring the variability of $t_{\rm sb}/D_{50}$ for a range of tills under similar stress conditions would further bolster our understanding of subglacial till flux.

4.2. Double-Valued Sediment Flux at Increasing Effective Stress

The "double-valued" trend we observe between N and $t_{\rm sb}$ contradicts the common assumption for subglacial settings that $Q_{\rm sed}$ increases monotonically with N. Although the rising limb occurs over a range of N that is particularly relevant to the dynamics of modern ice streams (Meyer et al., 2018), these stresses are substantially lower than pressure concentrations possible on the stoss side of bedform obstacles (Alley et al., 2021), which would fall within the decreasing limb of the relationship. This overall behavior, however, is consistent with the double-valued trend that Kasmalkar et al. (2021, Figure 3) reported from recent DEM experiments investigating till dynamics, and it aligns with the inverse relationship between N and $t_{\rm sb}$ reported for numerous physical and

HANSEN AND ZOET 11 of 18

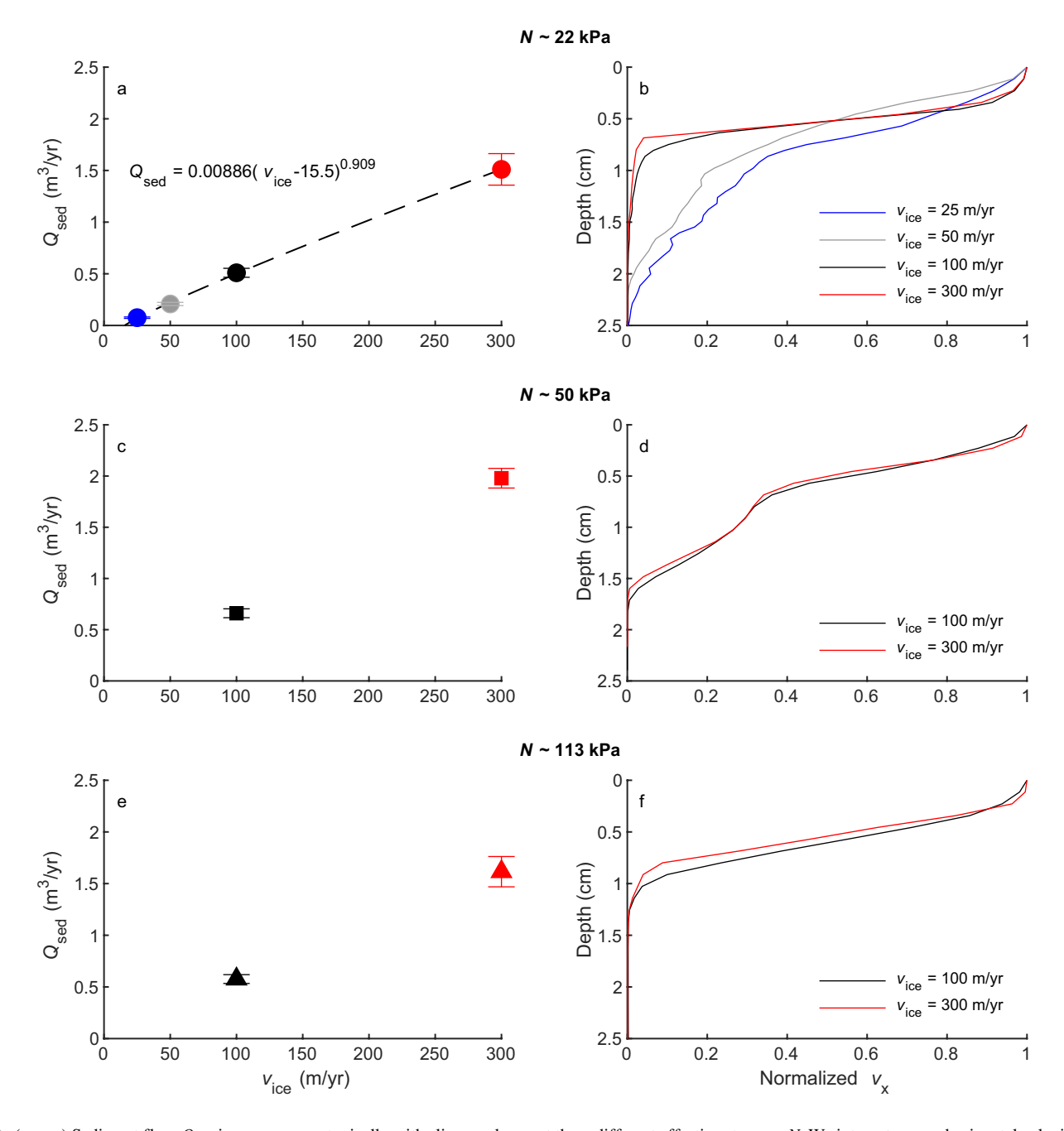


Figure 8. (a, c, e) Sediment flux, Q_{sed} , increases monotonically with slip speed, v_{ice} , at three different effective stresses, N. We integrate mean horizontal velocity, v_x , profiles (assuming unit width) with respect to vertical position to obtain Q_{sed} . Error bars show the standard deviation of the horizontal velocities, propagated through the numerical integration. (b, d, f) Mean horizontal velocity profiles for different slip speeds normalized by their maximum velocity. Depth represents inferred distance from the ice sole. Shared colors between Q_{sed} and normalized v_x plots were computed from the same selection of data. Dashed line and equation in panel (a) represent the best-fit curve computed through the linear regression.

numerical experiments within the fields of civil engineering and soft matter physics (Desrues & Viggiani, 2004; Gu et al., 2014, their Figure 10a), since the minimum stresses applied in these studies are generally too high to capture the rising limb we observe at low stresses ($N \sim 0$ –50 kPa).

Presumably, the disparity between our results and the assumptions of prevailing glaciological models exists because the constitutive laws commonly used to parameterize till deformation do not adequately capture the micromechanics controlling strain distribution at the grain scale. Current understanding is that the frictional response of glacial till to an applied load fits a Mohr Coulomb rheology, in which till strength is linearly proportional to

HANSEN AND ZOET 12 of 18

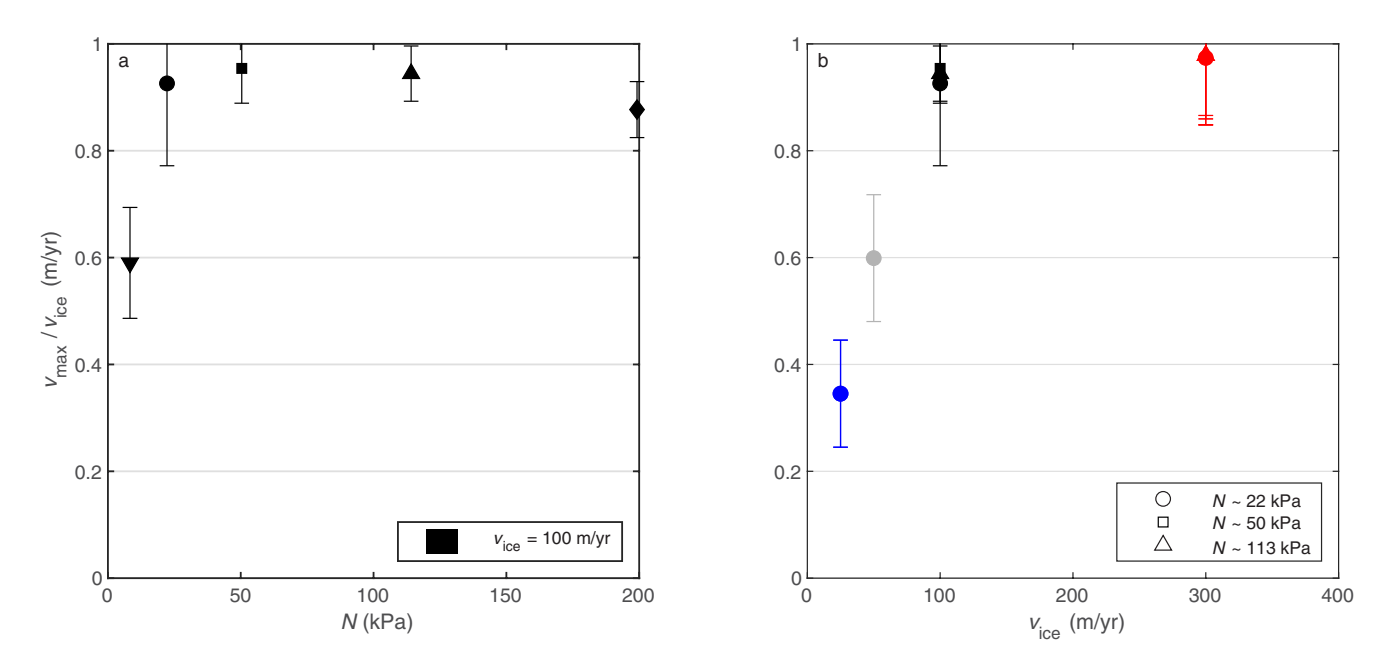


Figure 9. Observed relationships between (a) effective stress, N, and (b) ice velocity, v_{ice} , and the coupling between ice and till, expressed as the maximum horizontal velocity of till at the ice-bed interface, v_{max} , normalized by the speed of the ice, v_{ice} . Error bars denote standard deviation associated with each v_{max} normalized by v_{ice} . Horizontal error bars for N are smaller than the marker width.

N and independent of strain rate past a threshold sliding velocity (Iverson et al., 1998; Kamb, 1991). Conceptual models of till deformation conceived in a continuum framework capture these well-documented bulk frictional properties and suggest that depth of deformation scales with N (Iverson & Iverson, 2001). They do not, however, account for the mechanics of strain localization—a complex and ubiquitous process in geomaterials that defies simple parameterization (Tordesillas, 2007).

Heterogeneity in the stress field of granular materials, perhaps due to variable packing density or particle geometry, promotes instability and localized failure, which concentrates deformation in thin shear bands (Schall & Van Hecke, 2010). Once shear banding initializes, subsequent deformation can occur entirely within its confines, while the adjacent granular matrix remains static or moves as a rigid block (Rechenmacher et al., 2010). Strain distribution in a shear band is largely driven by formation and buckling of grain columns (or "force chains") that span its width (Rechenmacher, 2006). When a column fails, grains move past each other through the combined actions of sliding and rolling, depending on the force and torque applied. However, rotation rather than sliding appears to be the dominant style of movement within shear band boundaries once the residual state is reached with little rotation occurring in the adjacent granular matrix (Oda & Kazama, 1998; Zheng et al., 2019). Simulations with 2D DEMs that parameterize rolling resistance at particle contacts (Iwashita & Oda, 2000; Tang et al., 2016) and experimental observation (Amirrahmat et al., 2019) show that this rotation is a first-order control on shear band geometry. Free rolling particles produce wider shear bands with diffuse edges; whereas increased rotational resistance leads to thin zones of deformation characterized by steep rotational gradients at the boundaries. Rotational resistance is controlled by particle interlocking, which in turn is determined by the particle shape, surface texture, and the void ratio in the shear band (Hasan & Alshibli, 2010; Tian et al., 2020). Greater void ratio corresponds to a smaller number of contact points between interlocked grains and a decreased resistance to rolling. This point is particularly relevant in the context of our experimental results, since the critical state void ratio in a shear band is greater at low effective stresses (Imseeh et al., 2020). These particle kinematics suggest that the decreasing limb of the double-valued N-Q_{sed} relationship may arise due to suppressed grain rotation along shear band boundaries past the threshold N. This would lead to a decrease in shear band thickness with increasing effective stress, which is precisely the behavior we observe.

On the other hand, too much void space inhibits the transmission of forces across an unstable particle network since rotational resistance stabilizes particle columns (Gardiner & Tordesillas, 2004). This could explain the initial rise in $t_{\rm sb}$ and $Q_{\rm sed}$ with increasing N, since the larger void ratio and lower rolling resistance at low values

HANSEN AND ZOET 13 of 18



of N would limit the length of the stable particle columns. As rolling resistance increases with N, we anticipate the number of particles in a column—and thus $t_{\rm sb}$ —to increase concomitantly until a threshold N, at which point the balance between particle column stability and grain movement at the boundaries is conducive for a maximum thickness of the deforming layer. Further work is required to test this hypothesis.

4.3. Ice-Till Coupling Scales Velocity-Dependent Sediment Flux

Boulton and Dobbie (1998) reported that shear bands thickened at faster strain rates in split-cell ring shear experiments; however, we observe no such velocity-dependent increase in $t_{\rm sb}$. Conversely, $t_{\rm sb}$ decreased at faster velocities for some steps (Figure 7), but the difference in normalized flow profile is subtle for all stages with a well-developed shear band (Figures 8b, 8d and 8f). The above implies that friction at the contact between ice and till controls the positive relationship we observe between $v_{\rm ice}$ and $Q_{\rm sed}$. This finding aligns with previous soft matter physics research that suggest that the flow profile in granular material deforming in response to an overriding solid is nearly rate independent when normalized by the imposed shearing rate (Howell et al., 1999). Shear speed, however, influences the magnitude of the flow profile due to friction at the particulate-continuum interface. Coupling at this boundary has been shown to increase with the surface roughness and hardness properties of the continuum material (Frost et al., 2002). In the case of a perfectly coupled interface, grains at the boundary move at the speed of the contacting solid, and particle velocities decay with distance from the boundary. A perfectly smooth boundary on the other hand facilitates pure slip at the interface with no grain motion. Between these end-member scenarios, grains at the boundary are mobilized at a slower rate than the contacting medium, which is where our experiments largely reside.

Assuming a planar ice sole, roughness at the ice-bed interface is primarily controlled by the GSD of the till (Tulaczyk, 1999) and, if present, the thickness of a water film between ice and till, which submerges grains smaller than its depth (Creyts & Schoof, 2009). During basal slip, ice moves past exposed clasts through a combination of regelation and viscous creep, inducing a drag force against the stoss side of the particles that scales with slip speed, effective stress, and clast radius (Zoet & Iverson, 2020). For ice to mobilize a given clast, this drag must exceed the frictional strength of the till at grain contacts, at which point the mechanism accommodating forward motion shifts from slip to plowing. The velocity at which this transition occurs, u_t , is given by Zoet and Iverson's Equation 2. Larger clasts mobilize at slower speeds, and thus for a given effective stress, an increasing number of grains at increasingly smaller diameters begins to plow as ice velocity surpasses each grain's respective u_t . Their formulation (using the physical parameters they list for the same till) predicts that the minimum slip speed that will mobilize grains in our till (which has a maximum clast radius of ~4.7 mm) will be ~23.5 m/yr at $N \sim 22$ kPa and increases with increasing N. Notably, this prediction is ~1.5× greater than the speed at which we infer sediment flux to initiate for this value of N based on the x-intercept of the aforementioned power law fit in v_{ice} — Q_{sed} space (i.e., ~15.5 m/yr).

A larger percentage of plowing clasts at the ice-bed interface effectively increases the number of asperities protruding from the ice sole and thus, one anticipates a corresponding increase in coupling between ice and till, qualitatively similar to the velocity steps implemented at $N \sim 22$ kPa (Figure 9b). For velocity steps at $N \sim 50$ and ~ 113 kPa, the observation that coupling appears to have reached a maximum at 100 m/yr conflicts with Zoet and Iverson's model, which suggests that the transition velocity for a given clast size, and by extension $v_{\rm max}/v_{\rm ice}$, should occur at higher slip speeds for greater values of N. Furthermore, the interface was nearly coupled at $N \sim 22$ kPa and $v_{\rm ice} = 100$ m/yr, which coincides with a minimum mobilized clast radius of 3 mm in Zoet and Iverson's model—only $\sim 3\%$ of the grains in our till by volume. A confounding factor here could be the influence of sediment entrainment due to regelation infiltration or premelting effects (Meyer et al., 2018) on the frictional properties of the ice-bed interface. Both processes are more effective at higher values of N and could potentially alter the system beyond the mechanics explicitly considered in their formulation by progressively incorporating debris into basal ice. This seems possible since we intermittently observed a thin layer of debris-laden ice (O(10⁻³ m)) in the photographic time series (see Movie S2).

4.4. Glaciological Implications

The style of deformation recorded in these experiments illuminates key processes controlling till flux in modern subglacial environments and in relict glacial landscapes. Our main findings—a double-valued relationship

HANSEN AND ZOET 14 of 18



between N and Q_{norm} and a positive monotonic relationship between v_{ice} and Q_{sed} —provide a valuable metric to reassess long-standing assumptions, regarding the redistribution of sediment at the ice-bed interface during basal slip. Barchyn et al. (2016), for example, suggested that the elongation of soft-sediment bedforms is more efficient at faster sliding velocities due to increased rates of sediment transport from the stoss side (up-glacier) to the lee side (down-glacier) of the feature. In their heuristic model, this association arises due to the influence of two processes working in concert: (a) increased pressure on the stoss side of the bump, which causes till to deform faster at higher shear stresses due to an assumed viscous rheology for till and (b) increased rates of sediment entrainment on the stoss side and melt out on the lee. Our results point to a similar relationship between bedform elongation and slip speed, albeit through a different mechanism. If ice and till are coupled, our results suggest that the slip speed of basal ice is the dominant control on sediment flux in a deforming till bed. Though variations in effective stress influence the flow profile, the difference in Q_{sed} at low and high stresses is subtle compared to changes with slip speed. Rates of till transport along the areas of the bed with sustained low effective stresses or slower ice velocities will be depressed due to the reduced coupling at the interface and slower ice speeds. Conversely, the areas of the bed that experience sustained high stresses and fast velocities, such as the stoss side of bedform obstacles, will have elevated $Q_{\rm sod}$, so long as the driving stress exceeds the shear strength of the till. This should occur even at values of N past the point where shear bands begin to thin, since increased pressure induced on the adverse slope of the feature dewaters the ice-bed interface (Creyts & Schoof, 2009) and routes water around the bump (Alley et al., 2021). The corresponding reduction in film thickness increases the contact between ice and till on the stoss side, facilitating the transport of sediment near the ice sole down-glacier at a rate proportional to v_{ice} . In the lee, coupling would likely decrease due to the drop in ice pressure, perhaps accentuated by the presence of a water-filled cavity. This process would result in faster rates of till transport and deposition across the obstacle in response to faster slip speeds. Operating in conjunction with the entrainment/ melt out hypothesis offered by Barchyn et al. (2016), this mechanism may set up the necessary conditions for v_{ice} to drive bedform elongation.

This trade-off between areas with contrasting rates of subglacial till transport also has important implications for sliding dynamics. Basal friction is set by the composition of the bed (i.e., till vs. bedrock) and its topography, meaning these two parameters dictate the timing and rate of glacier retreat. Glaciers can be underlain by bedrock or completely mantled by a layer of till. However, most likely exist on a continuum between these two end-members with some subset of the bed-exposed rock and other parts partially covered with sediment (Muto et al., 2019). Empirical sliding laws that relate basal shear stress to slip speed for both hard and soft beds share a similar functional form (Helanow et al., 2021; Zoet & Iverson, 2020) but lead to very different predictions for drag at a given velocity due to the unique physics operating in each. Accounting for variable bed conditions is a necessary level of complexity when parameterizing basal friction (Koellner et al., 2019) but to do so requires constraint on the percentage of the ice-bed interface overlain by till. This question intrinsically rests on rates at which subglacial till can be deposited or evacuated from the system, which is set by the relationships we report here, as well as fluvial or debris entrainment processes. Increased rates of transport on the stoss side of obstacles or depressed rates in their lee imply that adverse facing slopes will be swept free of debris, rendering them hard-bedded, and areas in the lee may experience net deposition—in accordance with myriad field observations. The balance of these processes is effectively what determines if an area of the bed is hard or soft.

5. Conclusions

Soft-bed deformation experiments conducted with subglacial till show clear relationships between sediment flux and both effective stress and sliding velocity. In our experiments, changes in effective stress vary the thickness of a shear band near the ice sole in a double-valued manner, in which sediment flux increases with increasing effective stress to a maximum before reducing at higher stresses. When coupled at the ice-bed interface, the slip speed of basal ice scales the magnitude of the flow profile in deforming till and by extension, rates of till transport past a threshold sliding velocity. Increases in effective stress and sliding velocity both increase the coupling between ice and till. With respect to the influence of sliding velocity, this behavior appears to reflect a transition from form drag to skin friction in accordance with Zoet and Iverson's (2020) sliding law for glaciers on deformable beds. At a steady state, deformation was largely accommodated in a thin band near the ice sole, $\sim 0.7-2.5$ -cm thick, indicating that strain localization is an important consideration when parameterizing till deformation.

HANSEN AND ZOET 15 of 18



Data Availability Statement

The data and model files for these experiments are archived at the University of Wisconsin-Madison's Minds@ UW repository (Hansen & Zoet, 2022).

Acknowledgments

This work was supported by NSF 2048315. The authors thank Peter Sobel and Neal Lord for their work designing and constructing the ring shear apparatus. The authors thank the Wisconsin Geologic and Natural History Survey for conducting the laser diffraction analysis on the till used in these experiments.

References

- Alley, R., Lawson, D., Evenson, E., & Larson, G. (2003). Sediment, glaciohydraulic supercooling, and fast glacier flow. *Annals of Glaciology*, 36, 135–141. https://doi.org/10.3189/172756403781816121
- Alley, R. B., Anandakrishnan, S., Dupont, T. K., Parizek, B. R., & Pollard, D. (2007). Effect of sedimentation on ice-sheet grounding-line stability. Science, 315(5820), 1838–1841. https://doi.org/10.1126/science.1138396
- Alley, R. B., Holschuh, N., MacAyeal, D. R., Parizek, B. R., Zoet, L., Riverman, K., et al. (2021). Bedforms of Thwaites Glacier, West Antarctica: Character and origin. *Journal of Geophysical Research: Earth Surface*, 126(12), e2021JF006339. https://doi.org/10.1029/2021JF006339
- Alshibli, K. A., & Sture, S. (1999). Sand shear band thickness measurements by digital imaging techniques. *Journal of Computing in Civil Engineering*, 13(2), 103–109. https://doi.org/10.1061/(ASCE)0887-3801(1999)13:2(103)
- Amirrahmat, S., Druckrey, A. M., Alshibli, K. A., & Al-Raoush, R. I. (2019). Micro shear bands: Precursor for strain localization in sheared granular materials. *Journal of Geotechnical and Geoenvironmental Engineering*, 145(2), 04018104. https://doi.org/10.1061/(ASCE) GT.1943-5606.0001989
- Barchyn, T. E., Dowling, T. P., Stokes, C. R., & Hugenholtz, C. H. (2016). Subglacial bed form morphology controlled by ice speed and sediment thickness. *Geophysical Research Letters*, 43(14), 7572–7580. https://doi.org/10.1002/2016GL069558
- Barranger, Y., Doumalin, P., Dupré, J. C., & Germaneau, A. (2010). Digital image correlation accuracy: Influence of kind of speckle and recording setup. In *EPJ Web of Conferences* (Vol. 6, p. 31002). EDP Sciences. https://doi.org/10.1051/epjconf/20100631002
- Bart, P. J., Krogmeier, B. J., Bart, M. P., & Tulaczyk, S. (2017). The paradox of a long grounding during West Antarctic Ice Sheet retreat in Ross Sea. Scientific Reports, 7(1), 1–8. https://doi.org/10.1038/s41598-017-01329-8
- Bickel, V. T., Manconi, A., & Amann, F. (2018). Quantitative assessment of digital image correlation methods to detect and monitor surface displacements of large slope instabilities. *Remote Sensing*, 10(6), 865. https://doi.org/10.3390/rs10060865
- Boulton, G. S., & Dobbie, K. E. (1998). Slow flow of granular aggregates: The deformation of sediments beneath glaciers. *Philosophical Transactions of the Royal Society of London, Series A: Mathematical, Physical and Engineering Sciences*, 356(1747), 2713–2745. https://doi.org/10.1098/rsta.1998.0294
- Boulton, G. S., & Hindmarsh, R. C. A. (1987). Sediment deformation beneath glaciers: Rheology and geological consequences. *Journal of Geophysical Research*, 92(B9), 9059–9082. https://doi.org/10.1029/JB092iB09p09059
- Clark, C. D. (1993). Mega-scale glacial lineations and cross-cutting ice-flow landforms. Earth Surface Processes and Landforms, 18(1), 1–29. https://doi.org/10.1002/esp.3290180102
- Crammond, G., Boyd, S. W., & Dulieu-Barton, J. M. (2013). Speckle pattern quality assessment for digital image correlation. *Optics and Lasers in Engineering*, 51(12), 1368–1378. https://doi.org/10.1016/j.optlaseng.2013.03.014
- Creyts, T. T., & Schoof, C. G. (2009). Drainage through subglacial water sheets. *Journal of Geophysical Research*, 114(F4), F04008. https://doi.org/10.1029/2008JF001215
- Damsgaard, A., Egholm, D. L., Beem, L. H., Tulacyzk, S., Larson, N. K., Piotrowski, J. A., & Siegfried, M. R. (2016). Ice flow dynamics forced by water pressure variations in subglacial granular beds. *Journal of Geophysical Research*, 43(23), 12–165. https://doi.org/10.1002/2016GL071579
- Damsgaard, A., Egholm, D. L., Piotrowski, J. A., Tulaczyk, S., Larsen, N. K., & Tylmann, K. (2013). Discrete element modeling of subglacial sediment deformation. *Journal of Geophysical Research: Earth Surface*, 118(4), 2230–2242. https://doi.org/10.1002/2013JF002830
- Damsgaard, A., Goren, L., & Suckale, J. (2020). Water pressure fluctuations control variability in sediment flux and slip dynamics beneath glaciers and ice streams. *Communications Earth & Environment*, 1(1), 1–8. https://doi.org/10.1038/s43247-020-00074-7
- Desrues, J., & Viggiani, G. (2004). Strain localization in sand: An overview of the experimental results obtained in Grenoble using stereophotogrammetry. *International Journal for Numerical and Analytical Methods in Geomechanics*, 28(4), 279–321. https://doi.org/10.1002/nag.338
- Engelhardt, H., & Kamb, B. (1998). Basal sliding of ice stream B, West Antarctica. *Journal of Glaciology*, 44(147), 223–230. https://doi.org/10.3189/S0022143000002562
- Evans, D. J. A., Phillips, E. R., Hiemstra, J. F., & Auton, C. A. (2006). Subglacial till: Formation, sedimentary characteristics and classification. *Earth-Science Reviews*, 78(1–2), 115–176. https://doi.org/10.1016/j.earscirev.2006.04.001
- Fenistein, D., van de Meent, J. W., & van Hecke, M. (2004). Universal and wide shear zones in granular bulk flow. *Physical Review Letters*, 92(9), 094301. https://doi.org/10.1103/physrevlett.92.094301
- Fowler, A. C. (2010). The instability theory of drumlin formation applied to Newtonian viscous ice of finite depth. *Proceedings of the Royal Society A: Mathematical, Physical & Engineering Sciences*, 466(2121), 2673–2694. https://doi.org/10.1098/rspa.2010.0017
- Fowler, A. C., & Chapwanya, M. (2014). An instability theory for the formation of ribbed moraine, drumlins and mega-scale glacial lineations. Proceedings of the Royal Society A: Mathematical, Physical & Engineering Sciences, 470(2171), 20140185. https://doi.org/10.1098/rspa.2014.0185
- Frost, J. D., DeJong, J. T., & Recalde, M. (2002). Shear failure behavior of granular–continuum interfaces. *Engineering Fracture Mechanics*, 69(17), 2029–2048. https://doi.org/10.1016/S0013-7944(02)00075-9
- Gardiner, B. S., & Tordesillas, A. (2004). Micromechanics of shear bands. International Journal of Solids and Structures, 41(21), 5885–5901. https://doi.org/10.1016/j.ijsolstr.2004.05.051
- Gu, X., Huang, M., & Qian, J. (2014). Discrete element modeling of shear band in granular materials. *Theoretical and Applied Fracture Mechanics*, 72, 37–49. https://doi.org/10.1016/j.tafmec.2014.06.008
- Guizar-Sicairos, M., Thurman, S. T., & Fienup, J. R. (2008). Efficient subpixel image registration algorithms. *Optics Letters*, 33(2), 156–158. https://doi.org/10.1364/OL.33.000156
- Hansen, D. D., & Zoet, L. K. (2022). Data for "Characterizing sediment flux of deforming glacier beds" [Data set]. MINDS@UW. http://digital.library.wisc.edu/1793/82882
- Hasan, A., & Alshibli, K. A. (2010). Experimental assessment of 3D particle-to-particle interaction within sheared sand using synchrotron microtomography. Géotechnique, 60(5), 369–379. https://doi.org/10.1680/geot.2010.60.5.369
- Head, K. H. (1989). Soil technicians' handbook (No. 624.151 H4). Pentech Press.

HANSEN AND ZOET 16 of 18



- Helanow, C., Iverson, N. R., Woodard, J. B., & Zoet, L. K. (2021). A slip law for hard-bedded glaciers derived from observed bed topography. Science Advances, 7(20), eabe7798. https://doi.org/10.1126/sciadv.abe7798
- Hindmarsh, R. (1998). Drumlinization and drumlin-forming instabilities: Viscous till mechanisms. *Journal of Glaciology*, 44(147), 293–314. https://doi.org/10.3189/S002214300000263X
- Howell, D. W., Behringer, R. P., & Veje, C. T. (1999). Fluctuations in granular media. Chaos: An Interdisciplinary Journal of Nonlinear Science, 9(3), 559–572. https://doi.org/10.1063/1.166430
- Imseeh, W. H., Alshibli, K. A., & Al-Raoush, R. I. (2020). Discrepancy in the critical state void ratio of poorly graded sand due to shear strain localization. *Journal of Geotechnical and Geoenvironmental Engineering*, 146(8), 04020066. https://doi.org/10.1061/(ASCE) GT 1943-5606 0002280
- Iverson, N., Hooyer, T., & Baker, R. (1998). Ring-shear studies of till deformation: Coulomb-plastic behavior and distributed strain in glacier beds. *Journal of Glaciology*, 44(148), 634–642. https://doi.org/10.3189/S0022143000002136
- Iverson, N., Hooyer, T., Fischer, U., Cohen, D., Moore, P., Jackson, M., et al. (2007). Soft-bed experiments beneath Engabreen, Norway: Regelation infiltration, basal slip and bed deformation. *Journal of Glaciology*, 53(182), 323–340. https://doi.org/10.3189/002214307783258431
- Iverson, N., & Iverson, R. (2001). Distributed shear of subglacial till due to Coulomb slip. Journal of Glaciology, 47(158), 481–488. https://doi.org/10.3189/172756501781832115
- Iverson, N. R. (2010). Shear resistance and continuity of subglacial till: Hydrology rules. Journal of Glaciology, 56(200), 1104–1114. https://doi.org/10.3189/002214311796406220
- Iwashita, K., & Oda, M. (2000). Micro-deformation mechanism of shear banding process based on modified distinct element method. Powder Technology, 109(1-3), 192-205. https://doi.org/10.1016/S0032-5910(99)00236-
- Kamb, B. (1991). Rheological nonlinearity and flow instability in the deforming bed mechanism of ice stream motion. *Journal of Geophysical Research*, 96(B10), 16585–16595. https://doi.org/10.1029/91JB00946
- Kamb, B. (2001). Basal zone of the West Antarctic ice streams and its role in lubrication of their rapid motion. The West Antarctic Ice Sheet: Behavior and Environment, 77, 157–199. https://doi.org/10.1029/AR077p0157
- Kasmalkar, I., Damsgaard, A., Goren, L., & Suckale, J. (2021). Shear variation at the ice-till interface changes the spatial distribution of till porosity and meltwater drainage. *Journal of Geophysical Research: Earth Surface*, 126(12), e2021JF006460. https://doi.org/10.1029/2021JF006460
- King, E. C., Hindmarsh, R. C., & Stokes, C. R. (2009). Formation of mega-scale glacial lineations observed beneath a West Antarctic ice stream.

 Nature Geoscience, 2(8), 585–588. https://doi.org/10.1038/ngeo581
- Koellner, S., Parizek, B. R., Alley, R. B., Muto, A., & Holschuh, N. (2019). The impact of spatially-variable basal properties on outlet glacier flow. Earth and Planetary Science Letters, 515, 200–208. https://doi.org/10.1016/j.epsl.2019.03.026
- Meng, L., Jin, G., & Yao, X. (2006). Errors caused by misalignment of the optical camera axis and the object surface in the DSCM. *Journal of Tsinghua University*, 46(11), 1930.
- Meyer, C. R., Downey, A. S., & Rempel, A. W. (2018). Freeze-on limits bed strength beneath sliding glaciers. *Nature Communications*, 9(1), 1–6. https://doi.org/10.1038/s41467-018-05716-1
- Mickelson, D. M., & Syverson, K. M. (1997). Quaternary geology of Ozaukee and Washington counties, Wisconsin (Vol. 91). University of Wisconsin—Extension, Wisconsin Geological and Natural History Survey.
- Wisconsin Georgical and National Tristory Survey.
 Mueth, D. M., Debregeas, G. F., Karczmar, G. S., Eng, P. J., Nagel, S. R., & Jaeger, H. M. (2000). Signatures of granular microstructure in dense shear flows. *Nature*, 406(6794), 385–389. https://doi.org/10.1038/35019032
- Muto, A., Anandakrishnan, S., Alley, R. B., Horgan, H. J., Parizek, B. R., Koellner, S., et al. (2019). Relating bed character and subglacial morphology using seismic data from Thwaites Glacier, West Antarctica. Earth and Planetary Science Letters, 507, 199–206. https://doi.org/10.1016/j.epsl.2018.12.008
- Oda, M., & Kazama, H. (1998). Microstructure of shear bands and its relation to the mechanisms of dilatancy and failure of dense granular soils. *Géotechnique*, 48(4), 465–481. https://doi.org/10.1680/geot.1998.48.4.465
- Piotrowski, J. A., Mickelson, D. M., Tulaczyk, S., Krzyszkowski, D., & Junge, F. W. (2001). Were deforming subglacial beds beneath past ice sheets really widespread? *Quaternary International*, 86(1), 139–150. https://doi.org/10.1016/S1040-6182(01)00056-8
- Rattez, H., Shi, Y., Sac-Morane, A., Klaeyle, T., Mielniczuk, B., & Veveakis, M. (2020). Effect of grain size distribution on the shear band thickness evolution in sand. Géotechnique, 72(4), 1–14. https://doi.org/10.1680/jgeot.20.P.120
- Rechenmacher, A., Abedi, S., & Chupin, O. (2010). Evolution of force chains in shear bands in sands. Géotechnique, 60(5), 343–351. https://doi.org/10.1680/geot.2010.60.5.343
- Rechenmacher, A. L. (2006). Grain-scale processes governing shear band initiation and evolution in sands. *Journal of the Mechanics and Physics of Solids*, 54(1), 22–45. https://doi.org/10.1016/j.jmps.2005.08.009
- Rechenmacher, A. L., & Finno, R. J. (2004). Digital image correlation to evaluate shear banding in dilative sands. *Geotechnical Testing Journal*, 27(1), 13–22. https://doi.org/10.1520/GTJ11263J
- Rempel, A. W. (2008). A theory for ice-till interactions and sediment entrainment beneath glaciers. *Journal of Geophysical Research*, 113(F1), F01013. https://doi.org/10.1029/2007JF000870
- Roy, S., Scheper, B. J., Polman, H., Thornton, A. R., Tunuguntla, D. R., Luding, S., & Weinhart, T. (2019). Surface flow profiles for dry and wet granular materials by Particle Tracking Velocimetry; the effect of wall roughness. *The European Physical Journal E*, 42(2), 1–14. https://doi.org/10.1140/epje/i2019-11778-x
- Schall, P., & Van Hecke, M. (2010). Shear bands in matter with granularity. Annual Review of Fluid Mechanics, 42(1), 67–88. https://doi.org/10.1146/annurev-fluid-121108-145544
- Schoof, C. (2007). Pressure-dependent viscosity and interfacial instability in coupled ice-sediment flow. Journal of Fluid Mechanics, 570, 227–252. https://doi.org/10.1017/S0022112006002874
- Scott, L. R. (2011). Numerical analysis (p. 204). Princeton University Press.
- Simkins, L. M., Greenwood, S. L., & Anderson, J. B. (2018). Diagnosing ice sheet grounding line stability from landform morphology. *The Cryosphere*, 12(8), 2707–2726. https://doi.org/10.5194/tc-12-2707-2018
- Soltanbeigi, B., Altunbas, A., Gezgin, A. T., & Cinicioglu, O. (2020). Determination of passive failure surface geometry for cohesionless back-fills. Periodica Polytechnica: Civil Engineering, 64(4), 1100–1110. https://doi.org/10.3311/PPci.14241
- Stokes, C. R., & Clark, C. D. (2002). Are long subglacial bedforms indicative of fast ice flow? *Boreas*, 31(3), 239–249. https://doi.org/10.1111/j.1502-3885.2002.tb01070.x
- Tang, H., Dong, Y., Chu, X., & Zhang, X. (2016). The influence of particle rolling and imperfections on the formation of shear bands in granular material. *Granular Matter*, 18(1), 12. https://doi.org/10.1007/s10035-016-0607-3
- Tian, J., Liu, E., & He, C. (2020). Shear band analysis of granular materials considering effects of particle shape. Acta Mechanica, 231(11), 4445–4461. https://doi.org/10.1007/s00707-020-02771-y

HANSEN AND ZOET 17 of 18



- Tordesillas, A. (2007). Force chain buckling, unjamming transitions and shear banding in dense granular assemblies. *Philosophical Magazine*, 87(32), 4987–5016. https://doi.org/10.1080/14786430701594848
- Tulaczyk, S. (1999). Ice sliding over weak, fine-grained tills: Dependence of ice-till interactions on till granulometry. Special Papers Geological Society of America, 159–178. https://doi.org/10.1130/0-8137-2337-X.159
- Tulaczyk, S., Kamb, B., Scherer, R. P., & Engelhardt, H. F. (1998). Sedimentary processes at the base of a West Antarctic ice stream; constraints from textural and compositional properties of subglacial debris. *Journal of Sedimentary Research*, 68(3), 487–496. https://doi.org/10.2110/isr.68.487
- Tulaczyk, S., Kamb, W. B., & Engelhardt, H. F. (2000). Basal mechanics of ice stream B, West Antarctica: 1. Till mechanics. *Journal of Geophysical Research*, 105(B1), 463–481. https://doi.org/10.1029/1999JB900329
- Tulaczyk, S. M., Scherer, R. P., & Clark, C. D. (2001). A ploughing model for the origin of weak tills beneath ice streams: A qualitative treatment. Quaternary International, 86(1), 59–70. https://doi.org/10.1016/S1040-6182(01)00050-7
- Wu, P. K., Matsushima, K., & Tatsuoka, F. (2008). Effects of specimen size and some other factors on the strength and deformation of granular soil in direct shear tests. *Geotechnical Testing Journal*, 31(1), 45–64. https://doi.org/10.1520/GTJ10077
- Zheng, H., Wang, D., Tong, X., Li, L., & Behringer, R. P. (2019). Granular scale responses in the shear band region. *Granular Matter*, 21(4), 1–6. https://doi.org/10.1007/s10035-019-0958-7
- Zhu, H., Nguyen, H. N., Nicot, F., & Darve, F. (2016). On a common critical state in localized and diffuse failure modes. *Journal of the Mechanics and Physics of Solids*, 95, 112–131. https://doi.org/10.1016/j.jmps.2016.05.026
- Zoet, L. K., & Iverson, N. R. (2020). A slip law for glaciers on deformable beds. Science, 368(6486), 76–78. https://doi.org/10.1126/science.
- Zoet, L. K., Rawling, J. E., III, Woodard, J. B., Barrette, N., & Mickelson, D. M. (2021). Factors that contribute to the elongation of drumlins beneath the Green Bay Lobe, Laurentide Ice Sheet. *Earth Surface Processes and Landforms*, 46(13), 2540–2550. https://doi.org/10.1002/esp.5192

HANSEN AND ZOET 18 of 18